NANOSYSTEMS:
PHYSICS, CHEMISTRY, MATHEMATICS

Lomakin M.S., et al. *Nanosystems: Phys. Chem. Math.*, 2023, **14** (2), 242–253.
http://nanojournal.ifmo.ru

Original article

DOI 10.17586/2220-8054-2023-14-2-242-253

Pyrochlore phase in the Bi_2O_3–Fe_2O_3–WO_3–(H_2O) system: its formation by hydrothermal synthesis in the low-temperature region of the phase diagram

Makariy S. Lomakin[1,2,a], Olga V. Proskurina[1,3,b], Victor V. Gusarov[1,c]

[1]Ioffe Institute, St. Petersburg, Russia

[2]St. Petersburg Electrotechnical University "LETI", St. Petersburg, Russia

[3]St. Petersburg State Institute of Technology, St. Petersburg, Russia

[a]lomakinmakariy@gmail.com, [b]proskurinaov@mail.ru, [c]victor.v.gusarov@gmail.com

Corresponding author: Makariy S. Lomakin, lomakinmakariy@gmail.com

ABSTRACT The present paper investigates features of a (Bi, Fe, □)$_2$(Fe, W)$_2$O$_6$O$'_\delta$ cubic pyrochlore-structured phase (hereinafter BFWO) formation in the Bi_2O_3–Fe_2O_3–WO_3–(H_2O) system under the hydrothermal synthesis conditions at $T < 200$ °C and in the range of pH < 1. It was found that the BFWO phase is formed even when the amorphous precursor suspension is less than 100 °C. The BFWO phase particles have a conditionally spherical morphology and are polycrystalline. The dependency of the average particle size on the synthesis temperature correlates well with the dependency of the average crystallite size on this parameter: both values increase abruptly with an increase in the amorphous precursor suspension treatment temperature from 90 to 110 °C (from ∼140 and 70 nm to ∼180 and 90 nm, respectively), and with a further increase in the hydrothermal treatment temperature to 190 °C, they increase more smoothly (up to ∼210 and 110 nm, respectively). It was found that the average number of crystallites in a particle is ∼9 units regardless of the synthesis temperature, i.e. an increase in the BFWO phase particle size with the increasing temperature (in the considered temperature range) occurs mainly due to an increase in the size of their constituent crystallites.

KEYWORDS pyrochlore-structured phase, hydrothermal synthesis, phase formation, nanocrystals.

ACKNOWLEDGEMENTS The authors are grateful to D.P. Danilovich for assistance in performing the synthetic part of the work. XRD studies, SEM and EDXMA of samples were performed employing the equipment of the Engineering Center of the St. Petersburg State Institute of Technology (Technical University). The work was financially supported by the Russian Science Foundation (Project No. 20-63-47016).

FOR CITATION Lomakin M.S., Proskurina O.V., Gusarov V.V. Pyrochlore phase in the Bi_2O_3–Fe_2O_3–WO_3–(H_2O) system: its formation by hydrothermal synthesis in the low-temperature region of the phase diagram. *Nanosystems: Phys. Chem. Math.*, 2023, **14** (2), 242–253.

1. Introduction

The pyrochlore-structured complex oxide phases with variable composition are the objects of active researches in modern materials science [1–5]. Currently, there is an increased interest in ternary and more multicomponent pyrochlores containing d-elements, since this class of complex oxides has a set of promising physicochemical properties, among which are magnetic [6–8], electrophysical [9, 10], catalytic [11, 12] and optical [13–15] ones. In most of the presented works, the pyrochlore phase is obtained by the solid-state synthesis [6–11, 13], and only in some works, chemistry methods are used to obtain the pyrochlore phase, in particular, by the hydrothermal method [12, 14–16] or by co-precipitation followed by annealing [17, 18]. Important advantages of the hydrothermal method are the possibility of obtaining nanocrystalline materials and synthesizing oxide phases that are unstable at elevated temperatures [19, 20]. It should be noted that in most papers devoted to the hydrothermal synthesis of oxide nanomaterials, of hydrothermal treatment temperature is in the 100 to 250 °C range [21–24].

The hydrothermal treatment temperature and the pH value of the hydrothermal fluid are among the most important parameters of synthesis, since they affect the kinetics of the processes occurring under hydrothermal conditions, determining the crystalline phase precursor solubility and the reacting components diffusion rate. In this regard, the dimensional and morphological characteristics, as well as the chemical composition of the crystalline product, as a rule, strictly depend on these parameters [25–29].

In the Bi_2O_3–Fe_2O_3–WO_3–(H_2O) system, the cubic pyrochlore-structured phase (BFWO) was obtained by hydrothermal synthesis only at $T = 200$ °C [14, 16, 28] and 180 °C [15], while other isothermal regions of the phase diagram were not studied. In this work, the BFWO phase was obtained at lower temperatures of the amorphous precursor suspension treatment (90–190 °C).

The effect of the hydrothermal fluid pH on the chemical composition and size parameters of particles and crystallites of the BFWO phase was studied in [28]. It was shown that in the Bi_2O_3–Fe_2O_3–WO_3–(H_2O) system, the composition of the pyrochlore phase formed under hydrothermal conditions will coincide well with the nominal composition specified for the synthesis when the hydrothermal fluid pH is in the ∼2 to ∼5 range. The average particle and crystallite sizes in this pH range pass through an extremal value at pH ∼4–5, taking the smallest values at pH < 1. In other words, certain synthetic problems are inevitable when it is required to obtain the BFWO phase with the smallest possible particle and crystallite sizes and the composition specified for the synthesis at the same time. In this paper, a solution to this synthetic problem is proposed.

The aim of this work is to study features of the cubic pyrochlore-structured phase formation in the Bi_2O_3–Fe_2O_3–WO_3–(H_2O) system under the hydrothermal synthesis conditions at $T < 200$ °C and in the range of pH < 1.

2. Materials and Methods

2.1. Synthesis section

The synthesis procedure, which is the same for all samples, is described below, and Table 1 shows the values of the variable synthesis parameters (nominal composition specified for the synthesis and hydrothermal treatment temperature). To obtain one sample, **x** mmol of crystalline hydrate of bismuth (III) nitrate, $Bi(NO_3)_3{\cdot}5H_2O$ (puriss. spec.), and **y** mmol of crystalline hydrate of iron (III) nitrate, $Fe(NO_3)_3{\cdot}9H_2O$ (pur.), were dissolved in 8.3 ml of 6 M HNO_3 (puriss. spec.), after which 41.7 ml of distilled water was added to the resulting solution. Next, **z** mmol of sodium tungstate (VI) crystalline hydrate, $Na_2WO_4{\cdot}2H_2O$ (puriss. spec.), was dissolved in 50 ml of distilled water and the resulting solution was added dropwise into the acidic solution of bismuth and iron nitrates stirred with a magnetic stirrer at 800 rpm (∼30 mL of distilled water was then added there and used to rinse the beaker that had contained the sodium tungstate solution). After additional stirring at 1000 rpm for ∼1 h, the amorphous precursor suspension (pH < 1) obtained this way was transferred into Teflon chambers (∼80% filling) and placed in steel autoclaves, which were then put in a furnace heated up to **T**°C. After 24 h, the autoclaves were removed from the furnace and cooled in air. The resulting precipitates were separated from the mother liquor (it was poured out), rinsed with distilled water several times by decantation and dried at 70 °C for 24 h.

According to the synthesis procedure described above, four series of samples were obtained (series 1 is the main one, series 2, 3 and 4 are additional), the synthetic parameters of which are presented in Table. 1. When obtaining samples of series 1, the amorphous precursor suspension treatment temperature was varied, and the remaining series of samples were obtained in order to conduct additional studies. Series 2 was obtained in order to determine the effect of the amount of iron (III) in the nominal composition on the phase composition of the hydrothermal synthesis products; series 3 was produced for determining the phase composition of the precursor suspension dispersed phase before the hydrothermal treatment; while series 4 was produced for determining the phase composition of the hydrothermal synthesis products in the absence of some component in the nominal composition.

Samples of series 3 were obtained by the following procedure: when synthesizing samples of series 2: the suspensions remaining after autoclaves filling were centrifuged, the liquid phase poured out, and the resulting wet precipitate dried at 70 °C for 24 h. When obtaining samples of series 4, the volumes of mixed solutions remained constant, only the presence or absence of some component in the solutions varied. Rinsing of these samples after hydrothermal synthesis was carried out in isopropyl alcohol. The W+H^+ HTS 150 °C sample was synthesized by adding sodium tungstate (VI) solution to the nitric acid solution. The Bi+W HTS 150 °C sample was synthesized by adding sodium tungstate (VI) solution to the acidic bismuth (III) nitrate solution. The Fe+W HTS 150 °C sample was synthesized by adding sodium tungstate (VI) solution to the acidic iron (III) nitrate solution. The Bi+Fe HTS 150 °C sample was synthesized by adding 50 ml of distilled water to the acidic solution of bismuth (III) and iron (III) nitrates.

2.2. Characterization

The crystal structure of the obtained samples was analyzed by X-ray diffraction (XRD) using a Rigaku SmartLab 3 Powder X-ray Diffractometer (Rigaku Corporation, Japan). X-ray diffraction patterns (Co-K_α radiation (series 1 samples), Cu-K_α radiation (series 2, 3 and 4 samples), K_β filter) were recorded in the Bragg-Brentano geometry at room temperature. The observed peak parameters (the absolute intensity (I_{abs}), Bragg angle ($2\theta_{obs}$), full width at half maximum ($FWHM_{obs}$), and the integral width (β_{obs})) were determined using the Rigaku SmartLab Studio II software package. The same software package employed the method of fundamental parameters for plotting curves of the volume lognormal crystallite size distribution. The instrumental broadening ($FWHM_{instr}$) was corrected by using a standard recorded under similar conditions. The used standard was a single-crystal $SrTiO_3$ plate with a polished side perpendicular to the crystallographic direction [100]. According to the criterion that determines the type of peak profile [30], peaks in all samples were pseudo-Voigt, therefore, the calculation of the corrected value of the full width at half-height ($FWHM_{corr}$) was carried out taking into account the pseudo-Voigt peak shape (equation (1), [30]). The average crystallite size (D) and microstresses (ε_s) were calculated by the Williamson-Hall method for the case of pseudo-Voigt peaks observed in diffraction patterns (equation (8), [31]). The calculation was performed using the peaks with Miller indices of 311, 222,

TABLE 1. Obtained samples, nominal composition specified for the synthesis and synthesis temperature

Sample		Nominal composition	n(Bi) (**x**), mmol	n(Fe) (**y**), mmol	n(W) (**z**), mmol	**T**, °C
Series 1	$Fe_{1.5}$ HTS 90 °C	$Bi_{0.5}Fe_{1.5}WO_6$	3.5	10.5	7.0	90
	$Fe_{1.5}$ HTS 110 °C					110
	$Fe_{1.5}$ HTS 130 °C					130
	$Fe_{1.5}$ HTS 150 °C					150
	$Fe_{1.5}$ HTS 170 °C					170
	$Fe_{1.5}$ HTS 190 °C					190
Series 2	$Fe_{0.5}$ HTS 150 °C	$Bi_{0.5}Fe_{0.5}WO_{4.50}$	3.5	3.5	7.0	150
	$Fe_{1.5}$ HTS 150 °C	$Bi_{0.5}Fe_{1.5}WO_6$	3.5	10.5	7.0	
	$Fe_{3.0}$ HTS 150 °C	$Bi_{0.5}Fe_{3.0}WO_{8.25}$	3.5	21.0	7.0	
Series 3	$Fe_{0.5}$ no HTS_no rinsing	$Bi_{0.5}Fe_{0.5}WO_{4.50}$	3.5	3.5	7.0	–
	$Fe_{1.5}$ no HTS_no rinsing	$Bi_{0.5}Fe_{1.5}WO_6$	3.5	10.5	7.0	–
	$Fe_{3.0}$ no HTS_no rinsing	$Bi_{0.5}Fe_{3.0}WO_{8.25}$	3.5	21.0	7.0	–
Series 4	W+H^+ HTS 150 °C	WO_3	–	–	7.0	150
	Bi+W HTS 150 °C	$Bi_{0.5}WO_{3.75}$	3.5	–	7.0	
	Fe+W HTS 150 °C	$Fe_{1.5}WO_{5.25}$	–	10.5	7.0	
	Bi+Fe HTS 150 °C	$Bi_{0.5}Fe_{1.5}O_3$	3.5	10.5	–	

Note 1: Sample $Fe_{1.5}$ HTS 150 °C is included in both Series 1 and 2

400, 511, 440, 531, 622, 444, and 711, assuming $\lambda(\mathrm{Co}K_{\alpha 1})$ = 1.789001 Å, $K_{Scherrer} = 0.94$, and $K_{strain} = 4$. The use of the Williamson-Hall method for calculating the average crystallite size was justified by the presence of microstresses in all the samples, and the illegitimacy of using the traditional Scherrer's formula in this case.

Scanning electron microscopy (SEM) images and bulk elemental composition of the samples were obtained on a Tescan Vega 3 SBH scanning electron microscope (Tescan Orsay Holding, Czech Republic) with an Oxford Instruments Energy Dispersive X-ray Microanalysis (EDXMA) attachment. The relative number of elements was calculated using the AZtec software, and only such series of electronic transitions as Fe (K-series), Bi and W (L-series) were taken into account in the calculation. The characteristic emission spectra of each sample were accumulated from three sites with a total area of ∼9 mm^2, with a set of statistics for at least 2.5 million pulses at each site. The readings from each site were averaged, and the measurement error was determined at a confidence level of 0.95. The histograms of the volume particle size distribution were constructed on the basis of random 500-particle samples for each synthesized sample from series 1. The normal distribution curves describing the constructed histograms were plotted using the Origin 2018 software package.

3. Results and discussions

3.1. Chemical composition

The EDXMA data on the bulk chemical composition of the obtained samples are presented in Table 2. In all samples of series 1 and 2, the bismuth and tungsten atomic ratio generally corresponds to the nominal composition (except for the $Fe_{3.0}$ HTS 150 °C sample, in which there is a lack of tungsten), while the quantity of iron atoms in relation to these elements is much less, than in the nominal composition. The depletion of the bulk composition of these samples in iron (III) is apparently due to the fact that a significant part of this component remains in the cooled hydrothermal fluid, and therefore is removed during sediment rinsing. It should be noted that in the case of the $Fe_{1.5}$ HTS 190 °C sample, a certain excess of iron in its bulk composition relative to other samples of series 1 is due to the presence of another iron-containing phase in this sample (see 3.2. XRD analysis).

In addition, from the obtained data on the bulk composition of samples of series 3, it follows that, the distribution of components between the dispersed phase and the dispersion medium of the precursor suspension is very uneven: tungsten

TABLE 2. Bulk chemical composition of the obtained samples, in rel. at. units, according to the EDXMA data

Sample		Nominal composition	Bulk chemical composition		
			Bi/W±Δ	Fe/W±Δ	Bi/Fe±Δ
Series 1	$Fe_{1.5}$ HTS 90 °C	$Bi_{0.5}Fe_{1.5}WO_6$	0.50±0.02	0.40±0.01	1.26±0.06
	$Fe_{1.5}$ HTS 110 °C		0.54±0.04	0.35±0.02	1.57±0.03
	$Fe_{1.5}$ HTS 130 °C		0.56±0.03	0.36±0.01	1.53±0.12
	$Fe_{1.5}$ HTS 150 °C		0.53±0.05	0.37±0.03	1.41±0.06
	$Fe_{1.5}$ HTS 170 °C		0.54±0.02	0.39±0.01	1.38±0.05
	$Fe_{1.5}$ HTS 190 °C		0.54±0.02	0.57±0.06	0.96±0.08
Series 2	$Fe_{0.5}$ HTS 150 °C	$Bi_{0.5}Fe_{0.5}WO_{4.50}$	0.54±0.03	0.31±0.01	1.78±0.04
	$Fe_{1.5}$ HTS 150 °C	$Bi_{0.5}Fe_{1.5}WO_6$	0.53±0.05	0.37±0.03	1.41±0.06
	$Fe_{3.0}$ HTS 150 °C	$Bi_{0.5}Fe_{3.0}WO_{8.25}$	0.58±0.04	0.51±0.01	1.13±0.07
Series 3	$Fe_{0.5}$ no HTS_no rinsing	$Bi_{0.5}Fe_{0.5}W_{4.50}$	0.37±0.02	0.06±0.01	6.12±1.13
	$Fe_{1.5}$ no HTS_no rinsing	$Bi_{0.5}Fe_{1.5}WO_6$	0.32±0.02	0.15±0.01	2.08±0.12
	$Fe_{3.0}$ no HTS_no rinsing	$Bi_{0.5}Fe_{3.0}WO_{8.25}$	0.29±0.01	0.28±0.01	1.03±0.06
Series 4	W+H^+ HTS 150 °C	WO_3	–	–	–
	Bi+W HTS 150 °C	$Bi_{0.5}WO_{3.75}$	0.53±0.05	–	–
	Fe+W HTS 150 °C	$Fe_{1.5}WO_{5.25}$	–	0.54±0.01	–
	Bi+Fe HTS 150 °C	$Bi_{0.5}Fe_{1.5}O_3$	*no solid phase formed*		

(VI) is located predominantly in the solid phase, iron (III) – in the liquid phase, and bismuth (III) is distributed over these phases approximately equally. In the bulk composition of all samples of series 3, impurity amounts of sodium are also found, since the sediment was not rinsed during their preparation.

3.2. XRD analysis

Powder X-ray diffraction patterns of samples of series 1 are presented in Fig. 1. All the observed peaks refer to the cubic pyrochlore-structured BFWO phase (CSD 1961005, [16]), the only exception is the $Fe_{1.5}$ HTS 190 °C sample, the diffraction pattern of which demonstrates weak peaks from the α-Fe_2O_3 phase, in addition to peaks from the BFWO phase. The results of phase composition analysis of this sample indicate that the phase diagram of the Bi_2O_3–Fe_2O_3–WO_3–(H_2O) system has a two-phase region in which the BFWO phase coexists with the hematite phase in the region of compositions enriched in iron (III) oxide. The obtained experimental data can be useful for determining the boundary of the homogeneity region of the BFWO phase from the side iron oxide (III) – under hydrothermal conditions at low T (from 100 to $\sim$ 200°C). An increase in the hydrothermal fluid pH, according to the data on phase equilibria in the Fe_2O_3-H_2O system [32], will lead to an increase in the FeOOH$\rightarrow$ α-Fe_2O_3 transition temperature, which must be taken into account when studying the BFWO – α-Fe_2O_3 phase equilibrium region. It should be noted that the hematite phase may turn out to be nanocrystalline in the obtained samples, and a part of iron (III) may also be present in the amorphous phase located, for example, along the BFWO grain boundaries [33, 34]. In both described cases, X-ray diffraction does not make it possible to identify the iron-containing impurity phase in the presence of a complex oxide, in which the main scattering centers are “heavy” bismuth and tungsten atoms.

The unit cell parameter a of the BFWO phase is, within the error, the same for all samples of series 1 and is 10.33(1) Å, which indicates the absence of a noticeable change in the BFWO phase composition in these samples. It should be noted that the amorphous halo is not found on the presented diffraction patterns, from which it can be qualitatively concluded that the degree of the amorphous phase transformation into the crystalline BFWO phase is close to 1.

Fig. 2a shows the dependencies of the average crystallite size of the BFWO phase on the synthesis temperature, and Fig. 2b shows the curves of the volume lognormal crystallite size distribution based on peak 222 depending on the synthesis temperature (series 1 samples). The average crystallite size of the BFWO phase was estimated in two ways: (1) by the Williamson–Hall graphical method (Fig. 3), where the peaks corresponding to different crystallographic directions were included in the calculations, and (2) as a weighted average of the volume lognormal crystallite size

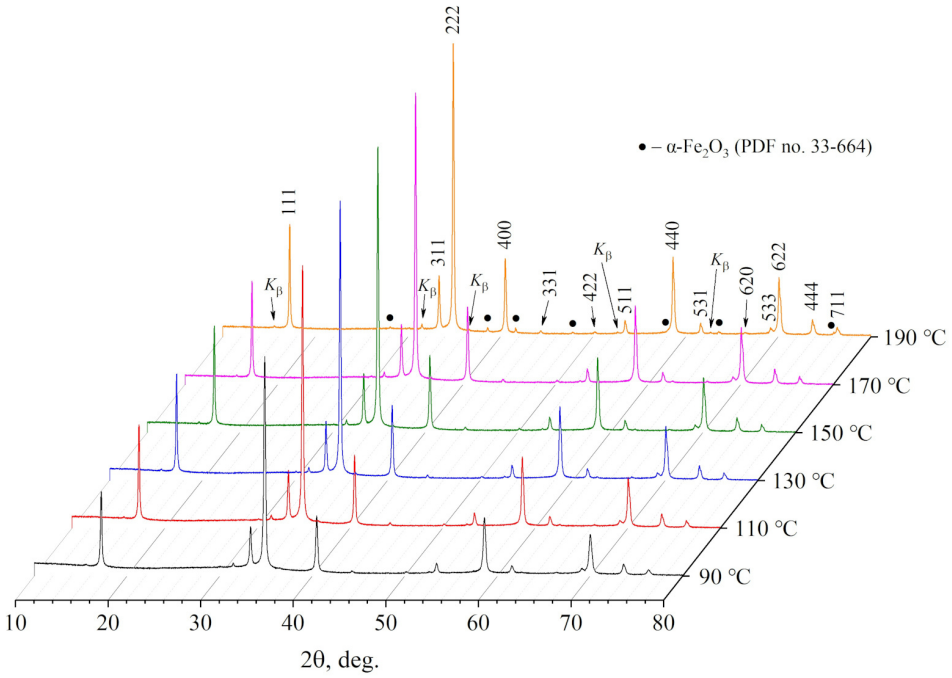

FIG. 1. XRD patterns (series 1 samples)

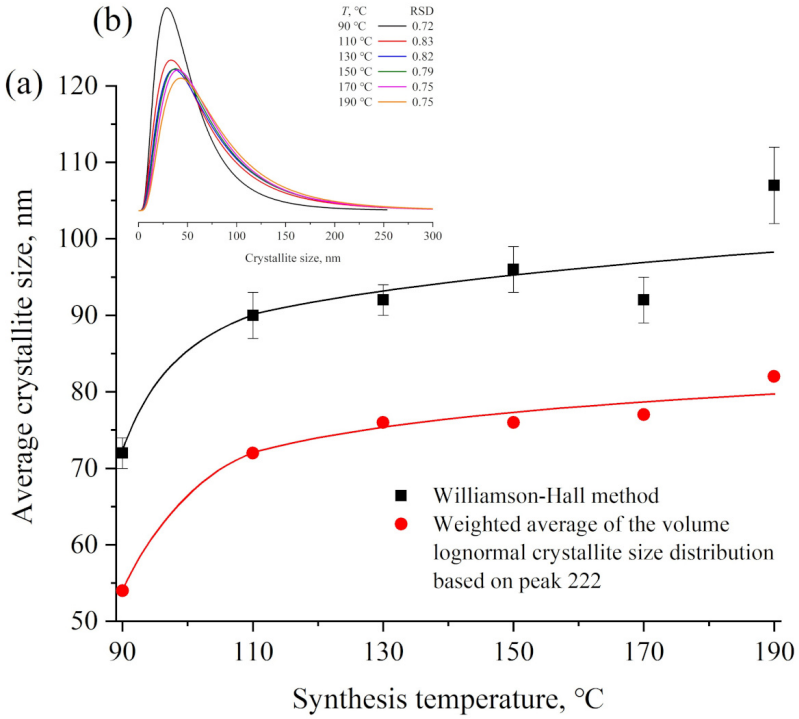

FIG. 2. (a) dependencies of the average crystallite size of the BFWO phase on the synthesis temperature and (b) curves of the volume lognormal crystallite size distribution based on peak 222 depending on the synthesis temperature (RSD – relative standard deviation) (series 1 samples)

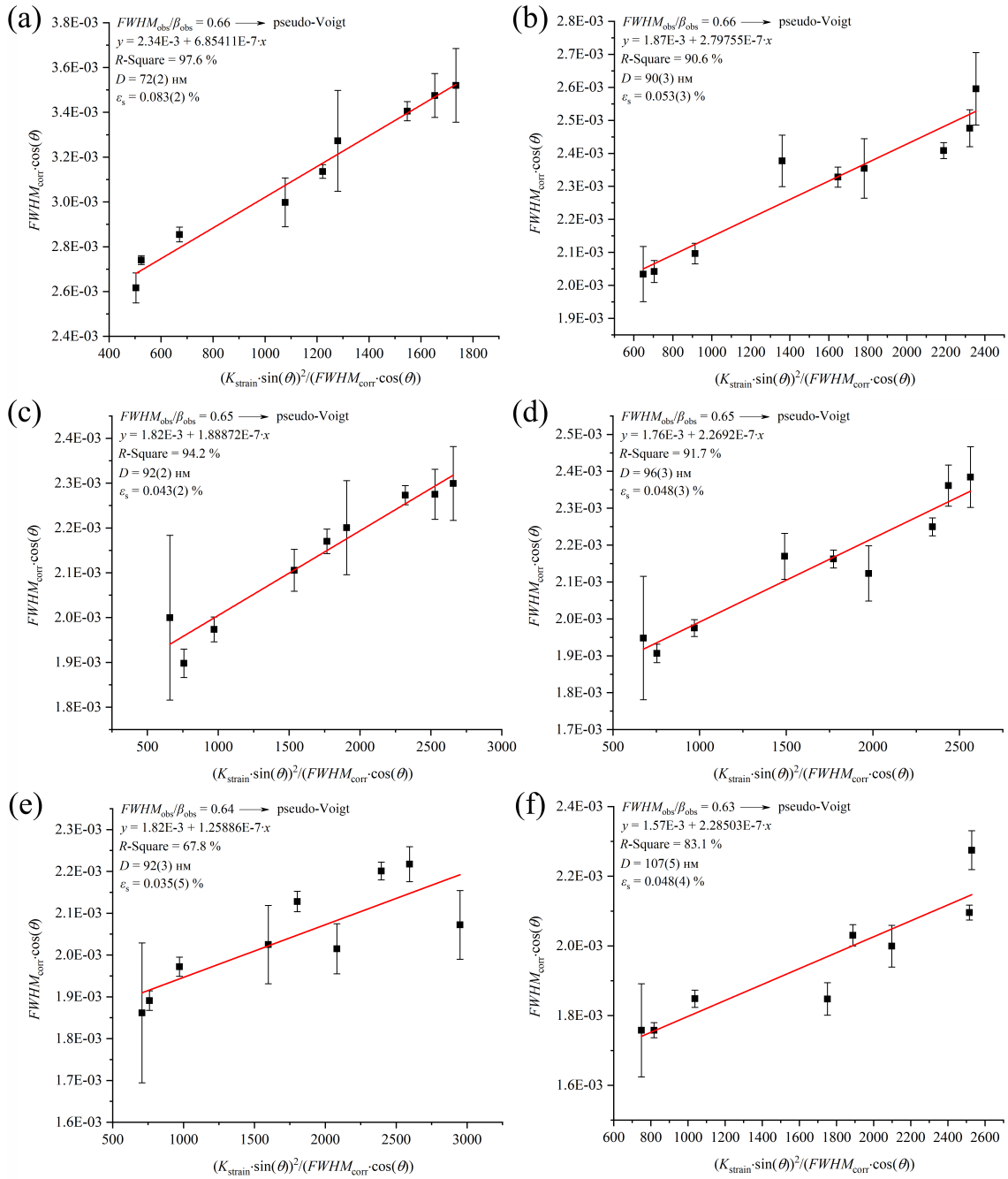

FIG. 3. Williamson-Hall plots for samples obtained at different synthesis temperatures (a (90 °C), b (110 °C), c (130 °C), d (150 °C), e (170 °C), f (190 °C)) (series 1 samples)

distribution based on peak 222. The average crystallite size calculated by method (1) turns out to be larger for each temperature taken than that calculated by method (2), however, both presented correlate well with each other. With an increase in the precursor suspension treatment temperature from 90 to 110 °C, the average in all crystallographic directions crystallite size increases abruptly from ∼70 to 90 nm, and the average in the [111] direction crystallite size from ∼55 to 70 nm; with a further increase in the hydrothermal treatment temperature to 190 °C, the average crystallite size increases more smoothly to ∼110 nm in the first case and to ∼80 nm in the second. It can be assumed that the differences in the average crystallite sizes calculated by the two methods are due either to some anisotropy of the crystallites or to the fact that the instrumental broadening of the device is taken into account in the first case using an external standard, while in the second case it is calculated based on the optical configuration of the device.

Powder X-ray diffraction patterns of samples of series 2, 3, and 4 are shown in Figs. 4,5,6, respectively. In the $Fe_{0.5}$ HTS 150 °C sample, in addition to peaks belonging to the BFWO phase (a = 10.33(1) Å), broad peaks are observed at 2θ angles (Cu-K_α radiation): 22.6, 28.1 (possibly Bi_2WO_6 (PDF no. 73-1126)), 36.4 and 55.3°, which indicate the presence of impurity amounts of an unidentifiable phase. The appearance of an impurity crystalline phase indicates that

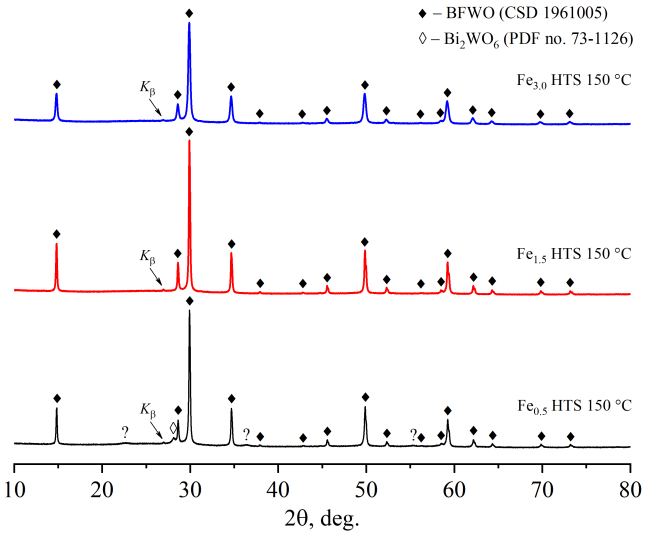

FIG. 4. XRD patterns (series 2 samples)

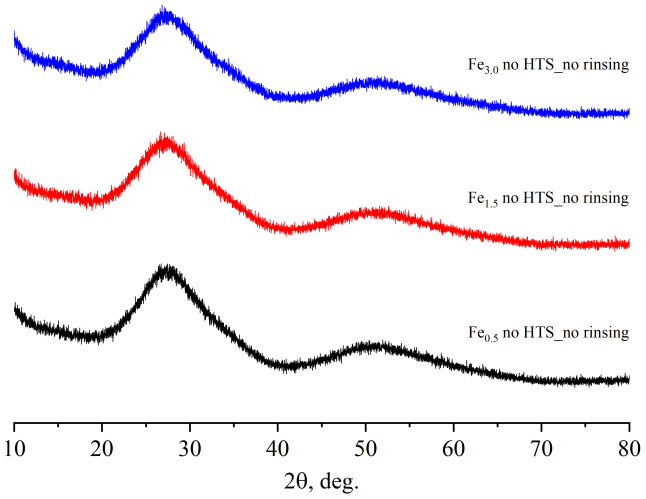

FIG. 5. XRD patterns (series 3 samples)

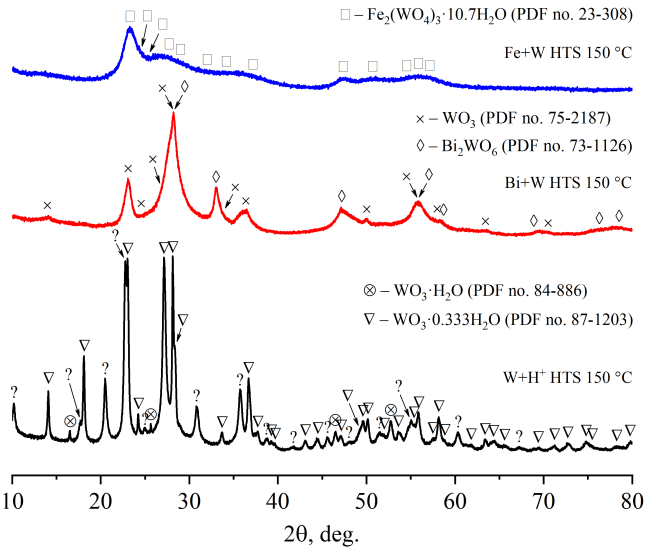

FIG. 6. XRD patterns (series 4 samples)

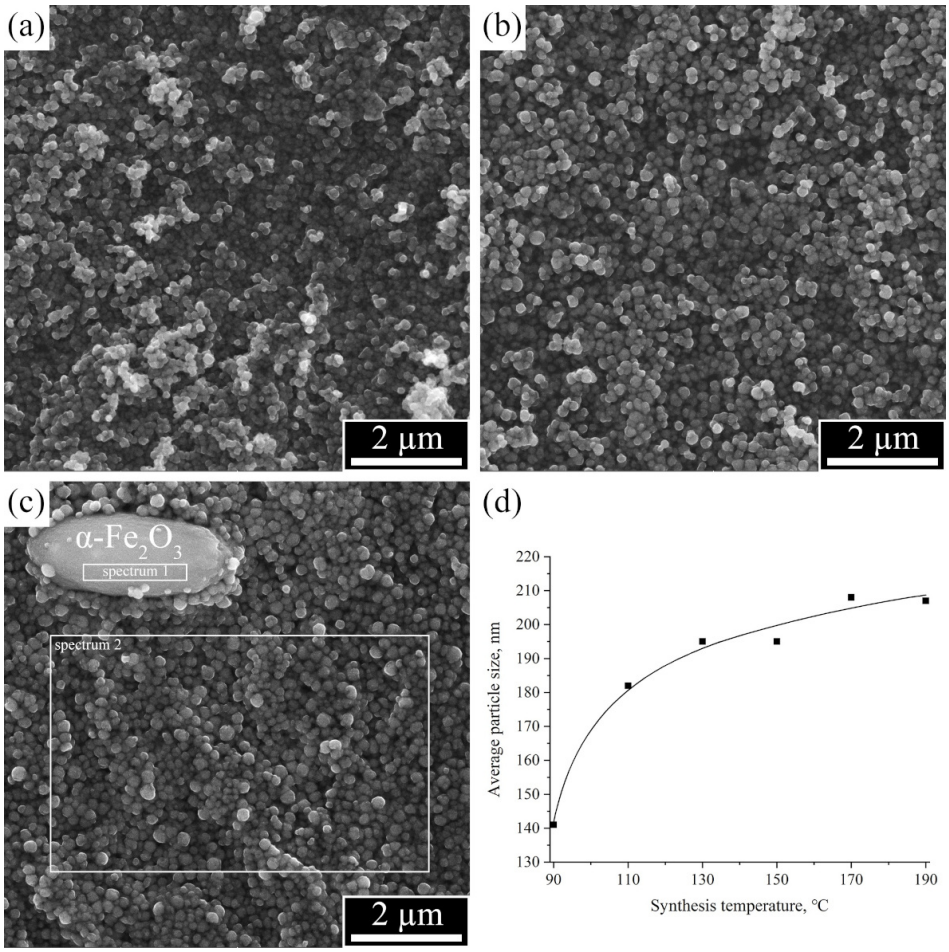

FIG. 7. (a (90 °C), b (110 °C), c (190 °C)) SEM data and (d) dependency of the BFWO phase average particle size on the synthesis temperature (series 1 samples)

the bulk composition of this sample, apparently is in the region of the phase diagram, which is more depleted in iron oxide, in comparison with the boundaries of the BFWO phase homogeneity region. In the $Fe_{1.5}$ HTS 150 °C and $Fe_{3.0}$ HTS 150 °C samples, the only crystalline phase is the BFWO phase (a = 10.33(1) Å and 10.35(1) Å, respectively), whose peaks in the second case turn out to be more broadened. The presented values of the BFWO phase unit cell parameter a indicate that the composition of this phase in the $Fe_{3.0}$ HTS 150 °C sample is more enriched in bismuth (III) than in other samples.

Thus, based on the data on the chemical and phase composition of the samples of series 1 and 2, it can be concluded that when the nominal composition of a sample contains a 2–4 times excess of iron (III) (relative to the stoichiometry of the BFWO phase homogeneity region) and the temperature of the precursor suspension hydrothermal treatment does not exceed ∼170 °C, there occurs the formation of the BFWO phase without impurities of other crystalline phases and with the Bi/W atomic ratio specified for the synthesis. In the case when the excess of iron (III) is ∼8 times, the composition of the forming BFWO phase turns out to be somewhat depleted in tungsten (VI) relative to the nominal composition specified for the synthesis. Otherwise, in the absence of an excess of iron (III), the bulk composition of the crystalline product formed as a result of hydrothermal synthesis (at pH < 1) is beyond the BFWO phase homogeneity region.

Powder X-ray diffraction patterns of samples of series 3 (Fig. 5) do not show any peaks from crystalline phases, which suggests that the dispersed phase of the precursor suspension is X-ray amorphous.

According to phase composition data (Fig. 6), no peaks characteristic of the pyrochlore-structured phase are observed in the samples of series 4. In the W+H^+ HTS 150 °C sample, most of the reflections belong to the $WO_3 \cdot 0.333H_2O$ (PDF no. 87-1203) and $WO_3 \cdot H_2O$ (PDF no. 84-886) phases, and the rest are not identified; in the Bi+W HTS 150 °C sample the Bi_2WO_6 (PDF no. 73-1126) and WO_3 (PDF no. 75-2187) phases are detected; in the Fe+W HTS 150 °C sample the $Fe_2(WO_4)_3 \cdot 10.7H_2O$ (PDF no. 23-308) phase is found while in the Bi+Fe HTS 150 °C sample the solid phase is absent.

3.3. SEM

The SEM data of samples of series 1 are presented in Fig. 7. In all single-phase samples of this series, only one morphological motif is observed, i.e. conditionally spherical particles, the size of which depends on the precursor suspension

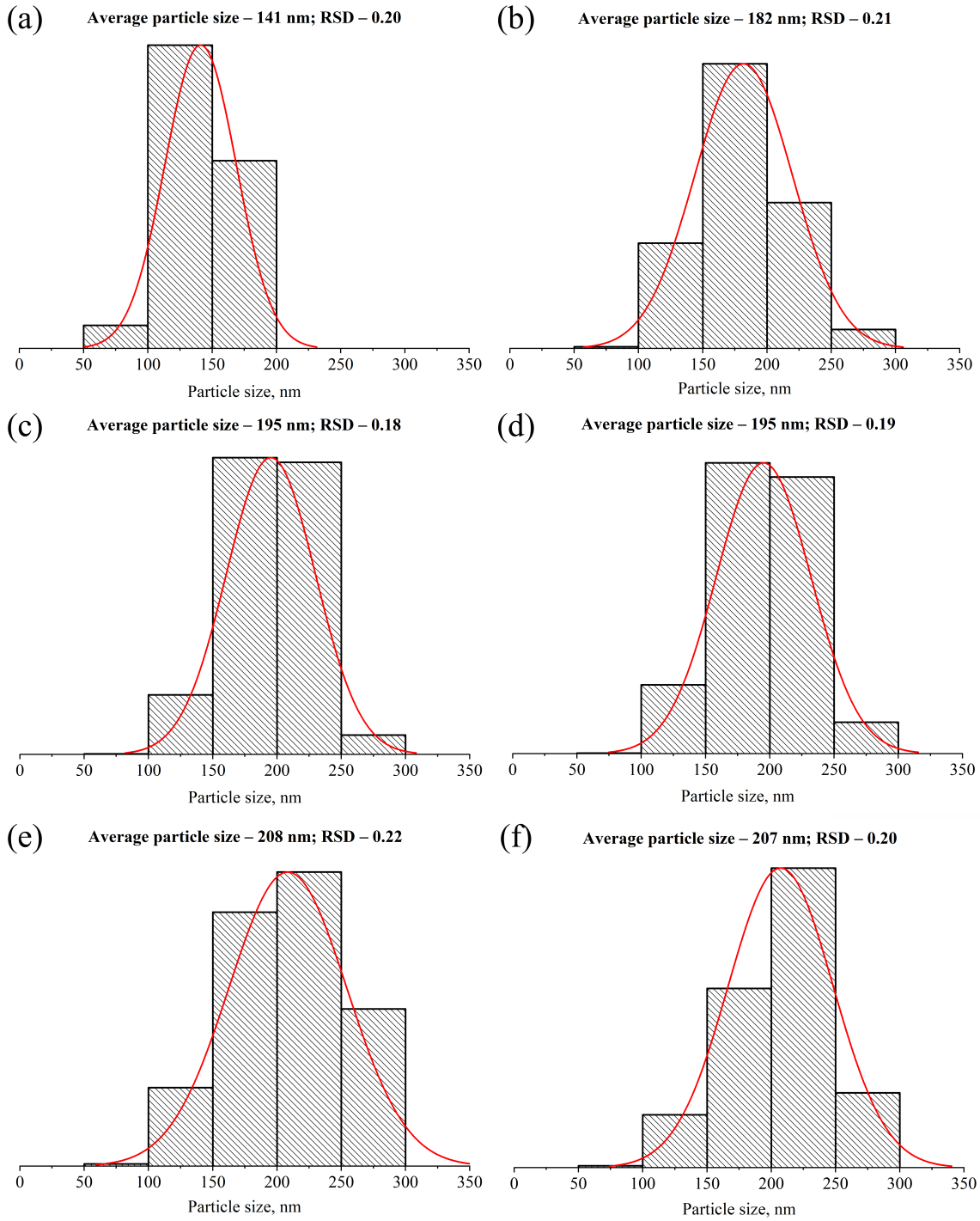

FIG. 8. Histograms and corresponding curves of the volume normal particle size distribution and normal distribution parameters, i.e. average size and RSD (relative standard deviation), for samples obtained at different synthesis temperatures (a (90 °C), b (110 °C), c (130 °C), d (150 °C), e (170 °C), f (190 °C)) (series 1 samples)

treatment temperature. In the $Fe_{1.5}$ HTS 190 °C sample, in addition to the BFWO phase particles, rare large particles resembling an elongated spheroid can be observed. According to the local EDXMA data, these large particles are the α-Fe_2O_3 phase (spectrum 1: $Bi_{0.73}Fe_{20.0}WO_{34.10}$), which peaks were detected in the diffraction pattern of the sample. It is interesting to note that the composition of the BFWO phase (spectrum 2: $Bi_{0.59}Fe_{0.38}WO_{4.46}$), obtained from a certain limited area that does not contain hematite particles, generally coincides with the bulk composition of single-phase samples of this series.

The constructed histograms of the volume particle size distribution are well described by the normal distribution function (Fig. 8), from which average particle sizes of the BFWO phase were determined. The dependency of the average particle size (Fig. 7d) on the synthesis temperature correlates well with the dependency of the average crystallite size on this parameter (Fig. 2): with an increase in the precursor suspension treatment temperature from 90 to 110 °C, the average particle size increases abruptly from ∼140 to 180 nm, and with a further increase in the hydrothermal treatment temperature to 190 °C, it increases more smoothly to ∼210 nm.

It should be noted that the BFWO phase particles observed in the micrographs are predominantly polycrystalline, which follows from a comparison of the average particle and crystallite sizes. Assuming that all particles and crystallites are conditionally spherical, and their diameters are equal to the average particle (Fig. 7d) and crystallite sizes (Fig. 2, Williamson-Hall method), respectively, the average number of crystallites in a particle will be ∼9 units regardless of the synthesis temperature. This fact may indicate that the increase in the BFWO phase particle size with temperature (in the considered temperature range) occurs mainly due to an increase in the size of their constituent crystallites. A jump-like increase in the average crystallite and, as a result, particle size following an increase in the precursor suspension treatment temperature from 90 to 110 °C may apparently, indicate a sharp increase in the amorphous precursor components solubility upon transition to the hydrothermal synthesis mode ($T > 100$ °C).

4. Conclusion

The characterized cubic pyrochlore-structured phase (BFWO) in the Bi_2O_3–Fe_2O_3–WO_3–(H_2O) system was obtained by hydrothermal synthesis at $T < 200$ °C and in the range of pH < 1. It was found that the BFWO phase is formed even when the precursor suspension treatment temperature is less than 100 °C, i.e. is beyond the lower limit of the hydrothermal synthesis. It was shown that when a sample nominal composition contains a 2–4 times excess of iron (III) (relative to the stoichiometry of the BFWO phase homogeneity region) and the precursor suspension hydrothermal treatment temperature does not exceeds ∼170 °C, then the formation of the BFWO phase without impurities of other crystalline phases and with the Bi/W atomic ratio specified for the synthesis is observed. In this case, the excess of iron (III) remains in the liquid phase and is removed from the system by rinsing the crystalline precipitate. With an increase in the hydrothermal treatment temperature to ∼190 °C, along with the pyrochlore phase, a hematite phase (α-Fe_2O_3) is formed. In the case of as much as the 8-time excess of iron (III), the composition of the forming BFWO phase turns out to be somewhat depleted in tungsten (VI) relative to the nominal composition specified for the synthesis. Otherwise, when there is no sufficient excess of iron (III) in the nominal composition of the sample, as a result of hydrothermal synthesis, multiphase mixtures containing the BFWO phase are formed, the bulk composition of which is in the region of the phase diagram that is more depleted in iron oxide, compared to the BFWO phase homogeneity region boundaries. It is shown that in the absence of any component in the nominal composition, a pyrochlore-structured phase is not formed as a result of hydrothermal synthesis.

It was established that the precursor suspension is dispersed phase X-ray amorphous, and the isothermal exposure for 24 h at all studied synthesis temperatures is sufficient to achieve complete transformation of the amorphous phase into the crystalline BFWO. The BFWO phase unit cell parameter a is 10.33(1) Å regardless of the synthesis temperature (the nominal composition being $Bi_{0.5}Fe_{1.5}WO_6$), which indicates that there is no noticeable change in the formed BFWO phase composition with temperature variation in the studied range.

The dependency of the average particle size on the synthesis temperature correlates well with the dependency of the average crystallite size on this parameter: both values increase abruptly with an increase in the amorphous precursor suspension treatment temperature from 90 to 110 °C while with a further increase in the hydrothermal treatment temperature to 190 °C, they increase more smoothly. Apparently, such a nature of the dependencies of these values on temperature may indicate a sharp increase in the solubility of the amorphous precursor components upon transition to the hydrothermal synthesis mode (T > 100 °C).

It was found that the average number of crystallites in a particle is ∼9 units regardless of the synthesis temperature. This fact may indicate that the increase in the BFWO phase particle size with increasing temperature (in the considered temperature range) occurs mainly due to an increase in the size of their constituent crystallites.

References

[1] Greedan J.E. Frustrated rare earth magnetism: spin glasses, spin liquids and spin ices in pyrochlore oxides. *Journal of Alloys and Compounds*, 2006, **408–412**, P. 444–455.

[2] Gardner J.S., Gingras M.J.P., Greedan J.E. Magnetic pyrochlore oxides. *Reviews of Modern Physics*, 2010, **82**(1), P. 53–107.

[3] Jitta R.R., Gundeboina R., Veldurthi N.K., Guje R., Muga V. Defect pyrochlore oxides: as photocatalyst materials for environmental and energy applications – a review. *Journal of Chemical Technology & Biotechnology*, 2015, **90**(11), P. 1937–1948.
[4] Anantharaman A.P., Dasari H.P. Potential of pyrochlore structure materials in solid oxide fuel cell applications. *Ceramics International*, 2021, **47**(4), P. 4367–4388.
[5] Wiebe C.R., Hallas A.M. Frustration under pressure: Exotic magnetism in new pyrochlore oxides. *APL Materials*, 2015, **3**(4), P. 041519.
[6] Ellert O.G., Egorysheva A.V., Gajtko O.M., Kirdyankin D.I., Svetogorov R.D. Highly frustrated Bi-Cr-Sb-O pyrochlore with spin-glass transition. *Journal of Magnetism and Magnetic Materials*, 2018, **463**, P. 13–18.
[7] Egorysheva A.V., Ellert O.G., Gaitko O.M., Brekhovskikh M.N., Zhidkova I.A., Maksimov Yu.V. Fluorination of Bi1.8Fe1.2SbO7 pyrochlore solid solutions. *Inorganic Materials*, 2017, **53**(9), P. 962–968.
[8] Babu G.S., Bedanta S., Valant M. Evidence of the spin glass state in $(Bi_{1.88}Fe_{0.12})(Fe_{1.42}Te_{0.58})O_{6.87}$ pyrochlore. *Solid State Communication*, 2013, **158**, P. 51–53.
[9] Jusoh F.A., Tan K.B., Zainal Z., Chen S.K., Khaw C.C., Lee O.J. Novel pyrochlores in the Bi_2O_3–Fe_2O_3–Ta_2O_5 (BFT) ternary system: synthesis, structural and electrical properties. *Journal of Materials Research and Technology*, 2020, **9**(5), P. 11022–11034.
[10] Zhuk N.A., Krzhizhanovskaya M.G., Sekushin N.A., Sivkov D.V., Muravyov V.A. Nb-doping effect on microstructure, thermal and dielectric properties of bismuth nickel tantalate pyrochlore. *Ceramics International*, 2023, **49**(2), P. 2934–2940.
[11] Valant M., Babu G.S., Vrcon M., Kolodiazhnyi T., Axelsson A.-K. Pyrochlore range from Bi_2O_3–Fe_2O_3–TeO_3 system for LTCC and photocatalysis and the crystal structure of new $Bi_3(Fe_{0.56}Te_{0.44})_3O_{11}$. *Journal of the American Ceramic Society*, 2012, **95**(2), P. 644–650.
[12] Playford H.Y., Modeshia D.R., Barney E.R., Hannon A.C., Wright C.S., Fisher J.M., Amieiro-Fonseca A., Thompsett D., O'Dell L.A., Rees G.J., Smith M.E., Hanna J.V., Walton R.I. Structural Characterization and Redox Catalytic Properties of Cerium(IV) Pyrochlore Oxides. *Chemistry of Materials*, 2011, **23**(24), P. 5464–5473.
[13] Zhuk N.A., Krzhizhanovskaya M.G., Koroleva A.V., Semenov V.G., Selyutin A.A., Lebedev A.M., Nekipelov S.V., Sivkov D.V., Kharton V.V., Lutoev V.P., Makeev B.A. Fe,Mg-Codoped Bismuth Tantalate Pyrochlores: Crystal Structure, Thermal Stability, Optical and Electrical Properties, XPS, NEXAFS, ESR, and ^{57}Fe Mössbauer Spectroscopy Study. *Inorganics*, 2023, **11**(1), P. 8.
[14] Lomakin M.S., Proskurina O.V., Sergeev A.A., Buryanenko I.V., Semenov V.G., Voznesenskiy S.S., Gusarov V.V. Crystal structure and optical properties of the Bi–Fe–W–O pyrochlore phase synthesized via a hydrothermal method. *Journal of Alloys and Compounds*, 2021, **889**, P. 161598.
[15] Lomakin M.S., Proskurina O.V., Levin A.A., Sergeev A.A., Leonov A.A., Nevedomsky V.N., Voznesenskiy S.S. Pyrochlore Phase in the Bi_2O_3–Fe_2O_3–WO_3–(H_2O) System: its Formation by Hydrothermal-Microwave Synthesis and Optical Properties. *Russian Journal of Inorganic Chemistry*, 2022, **67**(6), P. 820–829.
[16] Lomakin M.S., Proskurina O.V., Danilovich D.P., Panchuk V.V., Semenov V.G., Gusarov V.V. Hydrothermal Synthesis, Phase Formation and Crystal Chemistry of the pyrochlore/Bi_2WO_6 and pyrochlore/α-Fe_2O_3 Composites in the Bi_2O_3–Fe_2O_3–WO_3 System. *Journal of Solid State Chemistry*, 2020, **282**, P. 121064.
[17] Annamalai K., Radha R., Vijayakumari S., Kichanov S.E., Balakumar S. Insight into the investigation on nanostructured defect pyrochlore $Bi_{2-x}Fe_xWO_6$ and its photocatalytic degradation of mixed cationic dyes. *Materials Science in Semiconductor Processing*, 2022, **150**(2), P. 106961.
[18] Annamalai K., Radha R., Vijayakumari S., Balakumar S. High-temperature stabilized defect pyrochlore $Bi_{2-x}Fe_xWO_6$ nanostructures and their effects on photocatalytic water remediation and photo-electrochemical oxygen evolution kinetics. *Catalysis Science & Technology*, 2023, **13**(5), P. 1409–1424.
[19] Shandilya M., Rai R., Singh J. Review: hydrothermal technology for smart materials. *Advances in Applied Ceramics*, 2016, **115**(6), P. 354–376.
[20] Modeshia D.R., Walton R.I. Solvothermal synthesis of perovskites and pyrochlores: crystallisation of functional oxides under mild conditions. *Chemical Society Reviews*, 2010, **39**(11), P. 4303–4325.
[21] Ejsmont A., Goscianska J. Hydrothermal Synthesis of ZnO Superstructures with Controlled Morphology via Temperature and pH Optimization. *Materials*, 2023, **16**(4), P. 1641.
[22] Xiong D., Qi Y., Li X., Liu X., Tao H., Chen W., Zhao X. Hydrothermal synthesis of delafossite $CuFeO_2$ crystals at 100 C. *RSC Advances*, 2015, **5**, P. 49280–49286.
[23] Grendal O., Blichfeld A., Skjærvø S., van Beek W., Selbach S., Grande T., Einarsrud M.-A. Facile Low Temperature Hydrothermal Synthesis of $BaTiO_3$ Nanoparticles Studied by In Situ X-ray Diffraction. *Crystals*, 2018, **8**(6), P. 253.
[24] Zhang X., Liu X., Lu P., Wang L., Zhang Z., Wang X., Wang Z. Hydrothermal Synthesis of Lanthanide Stannates Pyrochlore Nanocrystals for Catalytic Combustion of Soot Particulates. *The Scientific World Journal*, 2015, **2015**, P. 254165.
[25] Almjasheva O.V., Popkov V.I., Proskurina O.V., Gusarov V.V. Phase formation under conditions of self-organization of particle growth restrictions in the reaction system. *Nanosystems: Physics Chemistry Mathematics*, 2022, **13**(2), P. 164–180.
[26] Almjasheva O.V., Lomanova N.A., Popkov V.I., Proskurina O.V., Tugova E.A., Gusarov V.V. The minimum size of oxide nanocrystals: phenomenological thermodynamic vs crystal-chemical approaches. *Nanosystems: Physics Chemistry Mathematics*, 2019, **10**(4), P. 428–437.
[27] Wang Y., Zhang S., Zhong Q., Zeng Y., Ou M., Cai W. Hydrothermal Synthesis of Novel Uniform Nanooctahedral $Bi_3(FeO_4)(WO_4)_2$ Solid Oxide and Visible-Light Photocatalytic Performance. *Industrial & Engineering Chemistry Research*, 2016, **55**(49), P. 12539–12546.
[28] Lomakin M.S., Proskurina O.V., Gusarov V.V. Influence of hydrothermal synthesis conditions on the composition of the pyrochlore phase in the Bi_2O_3–Fe_2O_3–WO_3 system, *Nanosystems: Physics Chemistry Mathematics*, 2020, **11**(2), P. 246–251.
[29] Proskurina O.V., Tomkovich M.V., Bachina A.K., Sokolov V.V., Danilovich D.P., Panchuk V.V., Semenov V.G., Gusarov V.V. Formation of Nanocrystalline $BiFeO_3$ under Hydrothermal Conditions. *Russian Journal of General Chemistry*, 2017, **87**(11), P. 2507–2515.
[30] Terlan B., Levin A.A., Börrnert F., Zeisner J., Kataev V., Schmidt M., Eychmüller A., A Size-Dependent Analysis of the Structural, Surface, Colloidal, and Thermal Properties of $Ti_{1-x}B_2$ (x =0.03–0.08) Nanoparticles. *European Journal of Inorganic Chemistry*, 2016, **21**, P. 3460–3468.
[31] Terlan B., Levin A.A., Börrnert F., Simon F., Oschatz M., Schmidt M., Cardoso-Gil R., Lorenz T., Baburin I.A., Joswig J.-O., Eychmüller A. Effect of Surface Properties on the Microstructure, Thermal, and Colloidal Stability of VB2 Nanoparticles. *Chemistry of Materials*, 2015, **27**(14), P. 5106–5115.
[32] Smith F.G., Kidd D.J. Hematite-goethite relation in neutral and alkaline solution under pressure. *American Mineralogist*, 1949, **34**(5), P. 403–412.
[33] Gusarov V.V., Egorov F.K., Ekimov S.P., Suvorov S.A. A Mossbauer study of the E kinetics of the film states formation at the interaction of magnesium and iron oxides. *The Journal of Physical Chemistry*, 1987, **61**(6), P. 1652–1654. (in Russian)
[34] Kirillova S.A., Almjasheva O.V., Panchuk V.V., Semenov V.G. Solid-phase interaction in ZrO_2–Fe_2O_3 nanocrystalline system. *Nanosystems: Physics Chemistry Mathematics*, 2018, **9**(6), P. 763–769.

Submitted 15 October 2022; revised 6 December 2022; accepted 10 December 2022

Information about the authors:

Makariy S. Lomakin – Ioffe Institute, 26, Politekhnicheskaya St., 194021, St. Petersburg, Russia; St. Petersburg Electrotechnical University "LETI", 5, Professor Popov St., 197376, St. Petersburg, Russia; ORCID0000-0001-5455-4541; lomakinmakariy@gmail.com

Olga V. Proskurina – Ioffe Institute, 26, Politekhnicheskaya St., 194021, St. Petersburg, Russia; St. Petersburg State Institute of Technology, 26, Moskovsky Ave., 190013, St. Petersburg, Russia; ORCID 0000-0002-2807-375X; proskurinaov@mail.ru

Victor V. Gusarov – Ioffe Institute, 26, Politekhnicheskaya St., 194021, St. Petersburg, Russia; ORCID 0000-0003-4375-6388; victor.v.gusarov@gmail.com

Conflict of interest: the authors declare no conflict of interest.